euronoise

Characterisation of the velocity distribution on rigid in-vitro upper airway replicas

Annemie Van Hirtum[a], Xavier Grandchamp[a], David Marx[b], Xavier Pelorson[a] and Helène Bailliet[b]

[a]Département Parole & Cognition, GIPSA-lab, 46, avenue Félix Viallet, 38031 Grenoble Cedex, France
[b]Laboratoire d'Etudes Aerodynamiques - CNRS, Bat K, 40 avenue du recteur Pineau, 86022 Poitiers, France
annemie.vanhirtum@gipsa-lab.inpg.fr

Qualitative and quantitative characterisation of the velocity distribution is an important aspect in order to study human speech production. Classical physical phonation models exploit quasi one-dimensional flow descriptions for which the velocity distribution is obtained from an analytical relationship depending on volume airflow velocity, geometry and pressure distribution. Therefore, 'in-vitro' validation and characterisation of simplified flow models is obtained straightforwardly by measuring the relevant quantities. More detailed and quantitative velocity predictions on the other hand, aiming e.g. to improve phonation modelling or to study turbulent sound production, require increased precision of the qualitative and quantitative characterisation of both the mean and fluctuating part of the velocity field. The current paper presents preliminary 'in-vitro' measurements of the velocity distribution obtained by hot film single sensor anemometry and two component Particle Image Velocimetry. Simplified rigid geometries are assessed in order to represent different geometries encountered in the upper airways. Besides qualitative results a first quantitative comparison between simulated and measured velocities is provided and discussed in case of round free jet development.

1 Introduction

Physical modelling of speech production is mostly dealing with phonation or voiced sound production denoting sounds involving auto-oscillations of the vocal folds due to the interaction with respiratory airflow as is the case for vowels. In general simplified models are preferred for physical phonation modeling in order to establish an unambiguous relationship between model parameters and 'in-vivo' or 'in-vitro' measurable quantities. Consequently, phonation models as the classical two mass model exploit quasi one-dimensional flow descriptions in order to estimate the pressure forces exerted on the vocal folds tissues [6]. These simplified flow models provide an analytical relationship between velocity distribution, volume airflow velocity, geometry and pressure distribution [2]. Therefore validation of the quasi one-dimensional flow models is obtained straightforwardly by measuring the relevant quantities [6, 2].
Although phonation involves a major part of human sound production, vocal folds auto-oscillations are a very particular and well localised sound source. Hence, a major part of fluid flow related phenomena and associated sounds are left untreated in classical studies dealing with physical phonation modelling. Moreover, the fluid flow through the upper airways is likely to become turbulent depending on flow and articulator conditions as illustrated in Figure 1. Consequently more detailed and

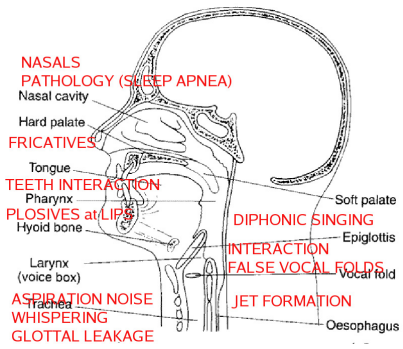

Figure 1: Upper airway articulators (small) and phenomena associated with turbulence (capitals).

quantitative flow model predictions aiming to improve phonation modelling or to study turbulent sound production require increased precision for qualitative and quantitative airflow characterisation. In addition to the characterisation of the smooth flow evolution associated with the main convective flow, the onset and development of turbulent flow requires the characterisation of the apparently random fluctuations of fluid motion superimposed to the mean flow.
In the current paper characterisation of the airflow is assessed by applying hot film single sensor anemometry and two dimensional Particle Image Velocimetry (PIV) to simplified mechanical replicas representing different portions of the upper airway and different articulator positions. Articulator configurations associated with turbulent flow development are considered [8, 9]. Besides qualitative results a quantitative comparison between simulated and measured velocities is provided and discussed axisymmetrical free jet development.

2 Velocity field characterisation

Measured velocity data are required in order to validate velocity field simulations and in order to estimate fluid mechanical and acoustical relevant quantities by means of integration or differentiation. In the following quantities of interest are outlined. Next the case of the round free jet is considered. Finally the limitations due to single sensor anemometry scanning and two-component PIV are briefly considered.

2.1 Quantities of interest

For incompressible flows $\nabla\mathbf{U} = 0$ holds where $\mathbf{U} = (U, V, W)$ denotes the velocity vector. In this case the Navier-Stokes equations can be rewritten in terms of the vorticity ω as:

$$\frac{\partial\omega}{\partial t} + \mathbf{U}\nabla\omega = \omega\nabla\mathbf{U} + \nu\nabla^2\omega \qquad (1)$$

where ν denotes the kinematic viscosity. Hence estimation of the vorticity field yields an important fluid mechanical quantity. The full velocity gradient tensor $\mathcal{G}$ is given as:

$$\mathcal{G} = \frac{d\mathbf{U}}{d\mathbf{X}} = \begin{bmatrix} \frac{\partial U}{\partial x} & \frac{\partial V}{\partial x} & \frac{\partial W}{\partial x} \\ \frac{\partial U}{\partial y} & \frac{\partial V}{\partial y} & \frac{\partial W}{\partial y} \\ \frac{\partial U}{\partial z} & \frac{\partial V}{\partial z} & \frac{\partial W}{\partial z} \end{bmatrix}, \qquad (2)$$

with $\mathbf{X} = (x, y, z)$ the position vector. The deformation tensor of eq. 2 can be decomposed into a symmetric

part and an antisymmetric part:

$$\frac{d\mathbf{U}}{d\mathbf{X}} = \begin{bmatrix} \frac{\partial U}{\partial x} & \frac{1}{2}\left(\frac{\partial V}{\partial x}+\frac{\partial U}{\partial y}\right) & \frac{1}{2}\left(\frac{\partial W}{\partial x}+\frac{\partial U}{\partial z}\right) \\ \frac{1}{2}\left(\frac{\partial U}{\partial y}+\frac{\partial V}{\partial x}\right) & \frac{\partial V}{\partial y} & \frac{1}{2}\left(\frac{\partial W}{\partial y}+\frac{\partial V}{\partial z}\right) \\ \frac{1}{2}\left(\frac{\partial U}{\partial z}+\frac{\partial W}{\partial x}\right) & \frac{1}{2}\left(\frac{\partial V}{\partial z}+\frac{\partial W}{\partial y}\right) & \frac{\partial W}{\partial z} \end{bmatrix} + \begin{bmatrix} 0 & \frac{1}{2}\left(\frac{\partial V}{\partial x}-\frac{\partial U}{\partial y}\right) & \frac{1}{2}\left(\frac{\partial W}{\partial x}-\frac{\partial U}{\partial z}\right) \\ \frac{1}{2}\left(\frac{\partial U}{\partial y}-\frac{\partial V}{\partial y}\right) & 0 & \frac{1}{2}\left(\frac{\partial W}{\partial y}-\frac{\partial V}{\partial z}\right) \\ \frac{1}{2}\left(\frac{\partial U}{\partial z}-\frac{\partial W}{\partial x}\right) & \frac{1}{2}\left(\frac{\partial V}{\partial z}-\frac{\partial W}{\partial y}\right) & 0 \end{bmatrix}. \tag{3}$$

The symmetric part represents the strain tensor with the elongational strains on the diagonal and the shearing strains on the off-diagonal, whereas the antisymmetric part contains only vorticity components. Hence eq. 2 can be expressed as:

$$\frac{d\mathbf{U}}{d\mathbf{X}} = \begin{bmatrix} \epsilon_{xx} & \frac{1}{2}\epsilon_{xy} & \frac{1}{2}\epsilon_{xz} \\ \frac{1}{2}\epsilon_{yx} & \epsilon_{yy} & \frac{1}{2}\epsilon_{yz} \\ \frac{1}{2}\epsilon_{zx} & \frac{1}{2}\epsilon_{zy} & \epsilon_{zz} \end{bmatrix} + \begin{bmatrix} 0 & \frac{\omega_z}{2} & \frac{-\omega_y}{2} \\ \frac{-\omega_z}{2} & 0 & \frac{\omega_x}{2} \\ \frac{\omega_y}{2} & \frac{-\omega_x}{2} & 0 \end{bmatrix}. \tag{4}$$

The Reynolds decomposition decomposes the velocity $\mathbf{U}(\mathbf{X},t)$ into its mean $\langle\mathbf{U}\rangle$ and fluctuation $\mathbf{u} = (u_1, u_2, u_3)$:

$$\mathbf{u}(\mathbf{X},t) \equiv \mathbf{U}(\mathbf{X},t) - \langle\mathbf{U}(\mathbf{X},t)\rangle \tag{5}$$

The mean momentum equation is then expressed by the Reynolds equations

$$\frac{\overline{D}\langle U_j\rangle}{\overline{D}t} = \nu\nabla^2\langle U_j\rangle - \frac{\partial\langle u_i u_j\rangle}{\partial x_i} - \frac{1}{\rho}\frac{\partial\langle p\rangle}{\partial x_j}, \tag{6}$$

where the term $\langle u_i u_j\rangle$ denotes the Reynolds stresses. Together with the Poisson equation for $\langle p\rangle$,

$$-\frac{1}{\rho}\nabla^2\langle U_j\rangle = \frac{\partial\langle U_i\rangle}{\partial x_j}\frac{\partial\langle U_j\rangle}{\partial x_i} + \frac{\partial^2\langle u_i u_j\rangle}{\partial x_i \partial x_j}, \tag{7}$$

the Reynolds equations provides 4 equations for the four unknows $\langle U\rangle$, $\langle p\rangle$ and in addition the unknown Reynolds stresses. Therefore the set of equations is unclosed. The diagonal components of the symmetric Reynolds stress tensor $\langle u_i u_j\rangle$,

$$\langle u_i u_j\rangle = \begin{bmatrix} \langle u_1^2\rangle & \langle u_1 u_2\rangle & \langle u_1 u_3\rangle \\ \langle u_1 u_2\rangle & \langle u_2^2\rangle & \langle u_2 u_3\rangle \\ \langle u_1 u_3\rangle & \langle u_2 u_3\rangle & \langle u_3^2\rangle \end{bmatrix}, \tag{8}$$

are normal stresses whereas the off-diagonal components are shear stresses. Half the trace of the Reynolds stress tensor defines the turbulent kinetic energy $k(\mathbf{X},t)$:

$$k(\mathbf{X},t) \equiv \frac{1}{2}\langle\mathbf{u}\cdot\mathbf{u}\rangle = \frac{1}{2}\langle u_i u_i\rangle. \tag{9}$$

So, obviously the Reynolds stresses are an important physical quantity appearing among others in Lighthill's stress tensor whose elements T_{ij} reduces for an inviscid and isentropic flow to

$$T_{ij} = \rho\langle u_i u_j\rangle. \tag{10}$$

2.2 Round free jet

The turbulent round free jet at the exit of a circular tube with length L and diameter d is characterised by self-similar behaviour of the mean velocity field as well as the Reynolds stresses [7]. The mean centerline velocity $U_c(x)$ is expected to decrease proportional to x^{-1} while the mean radial profiles $U(x,y)$ scales with the centerline velocity:

$$\frac{U_0}{U_c} = \frac{1}{K}\frac{x-x_0}{d} \text{ and } \frac{U(x,y)}{U_c(x)} = e^{-\alpha\eta^2} \tag{11}$$

with K centerline decay rate, $\eta = \frac{y}{x-x_0}$, U_0 the velocity at the tube exit, x_0 virtual origin, x the flow direction, y the transverse radial direction and the model parameter α derived from the radial spreading rate S as $\alpha = ln(2)/S^2$ often yielding α=94 for a round free jet. Besides the mean velocity field the turbulence statistics expressed by root mean square (rms) $u' = \sigma \equiv \langle u^2\rangle^{1/2}$ and higher moments, i.e. skewness $S_u \equiv \langle u^2\rangle^3/\sigma^3$ and kurtosis $K \equiv \langle u^2\rangle^4/\sigma^4$, approach Gaussian values in the self-similar region.
A turbulent viscosity $\nu_T(x,y) = y_{1/2}U_c(x)\hat{\nu}_T(\eta)$ can be estimated from S and jet half width $y_{1/2}$ as

$$\nu_T(x,y) = y_{1/2}(x)U_c(x)\hat{\nu}_T(\eta) \text{ with } \hat{\nu}_T(\eta) = \frac{S}{8(\sqrt{2}-1)}. \tag{12}$$

The assumption of turbulent viscosity $\nu_T(x,t)$ allows to overcome the closure problem and to estimate the shear stress from the mean velocity field,

$$\langle u_1 u_2\rangle = -\nu_T\frac{\partial\langle U\rangle}{\partial r}. \tag{13}$$

The Reynolds stress tensor for a two-dimensional flow statistically invariant under reflections of the z coordinate axis reduces to

$$\langle u_i u_j\rangle = \begin{bmatrix} \langle u_1^2\rangle & \langle u_1 u_2\rangle & 0 \\ \langle u_1 u_2\rangle & \langle u_2^2\rangle & 0 \\ 0 & 0 & \langle u_3^2\rangle \end{bmatrix}. \tag{14}$$

Furthermore the velocity spectra inform on the energy scales. A simple power law is applied in order to model the energy spectra $E(k)$ as:

$$E(k) = \frac{C_1}{\left(1+\frac{k}{C_2}\right)^n}. \tag{15}$$

with wavenumber k and $C_{1,2}$ model constants. Exponent n set to $n = 5/3$ and $n = 3$ corresponds to Kolgomorovs and Kraichnans law respectively indicating the inertial and decay portion of the spectra respectively [4].

2.3 Measurement limitations

Single sensor or one-componenet (1D) anemometry or two-component PIV (2D PIV) provides at most the x and y velocity components. Consequently this data can only be differentiated with respect to the x and y directions. Therefore only a few terms of the deformation tensor, eq. 4, can be estimated, i.e. vorticity component ω_z normal to the light sheet in case of 2D PIV along with the in-plane shearing ϵ_{xy} and extensional strains ϵ_{xx} and ϵ_{yy}. Remark that for an incompressible flow, $\nabla\mathbf{U} = 0$, the third in-plane extensional strain can be estimated as $\epsilon_{zz} = -(\epsilon_{xx} + \epsilon_{yy})$. Following [10] vortices appear

for non-real eigenvalues of the reduced velocity gradient tensor $\mathcal{G}$:

$$\mathcal{G} = \frac{d\mathbf{U}}{d\mathbf{x}} = \begin{bmatrix} \frac{\partial U}{\partial x} & \frac{\partial V}{\partial x} \\ \frac{\partial U}{\partial y} & \frac{\partial V}{\partial y} \end{bmatrix}. \quad (16)$$

The discriminant λ_2 of non-real eigenvalues of the velocity tensor $\mathcal{G}$ separates vortices from other patterns:

$$\lambda_2 = (trace\,\mathcal{G})^2 - 4\,det\,(\mathcal{G}) \quad (17)$$

3 Experimental setup

Qualitative and quantificative characterisation of the instantaneous velocity field is experimentally assessed with 1D anemometry and 2D PIV [5, 1]. PIV has the advantage to inform non-intrusively on large parts of flow fields while anemometry allows direct measurement of the velocity distribution. Mechanical 'in-vitro' replicas with different degree of complexity and typical airflow conditions encountered during speech production are briefly described in the next section.

3.1 Experimental conditions

The upper airway geometry stretches from the larynx up to the lips as depicted in Fig. 1. Airflow conditions in the upper airways during speech production are characterised in terms of relevant non-dimensional numbers as: Reynolds Re$\approx O(10^3)$, Mach Ma $\approx O(10^{-2})$, Strouhal Sr $\approx O(10^{-2})$ and the airflow is assumed to be incompressible [6, 9]. The vocal tract length ranges from 7 up to 18 cm depending on age and morphology whereas position and degree of constrictions depend on the articulators configuration. Rigid and deformable 'in-vitro' mechanical replicas with different degree of complexity are developed in order to study the flow behaviour and the influence of mechanical conditions, e.g. [2, 3, 6]. In the following severely simplified rigid and deformable replicas are considered as illustrated in Fig. 2 [6, 2].

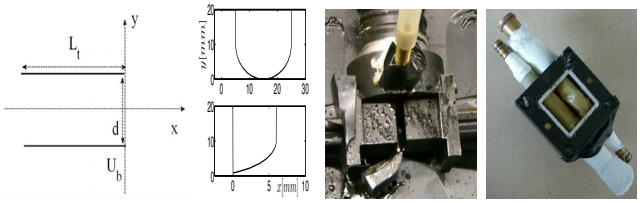

Figure 2: Schematic overview of some 'in-vitro' geometries: circular tube, exemplary rigid downstream constrictions with or without forced movement (y dimension), front view deformable replica.

3.2 Single sensor anemometry

A jet is generated in a flow facility consisting of an air compressor (Atlas Copco GA7) followed by a manual valve and pressure regulator (Norgren type 11-818-987) enabling to provide constant air pressure. A constant temperature anemometer system (IFA 300) is available in order to perform flow velocity measurements. The hot-film is calibrated against mean velocities given by the flow meter. A fourth polynomial law is fitted to the anemometer output voltage in order to convert measured voltage to velocity with an accuracy of 0.1m/s. Longitudinal (x) and radial (y) velocity profiles are obtained by moving a single sensor hot film (TSI 1201-20) with a diameter of 50.8μm and a working length of 1.02mm using a two-dimensional stage positioning system (Chuo precision industrial co. CAT-C, ALS-250-C2P and ALS-115-E1P) with accuracy $\Delta x = 4$ and $\Delta y = 2\mu$m. At each position velocity data are acquired at 30kHz for 3s consecutively.

3.3 Two component PIV (2D PIV)

Smoke tracer particles with a mean diameter inferior to 1μm are added to the airflow. A plane within the flow is illuminated twice by means of a laser (dual-YAG) light sheet whereas the time delay is adapted depending on the mean flow velocity and the magnification of imaging. It is assumed that the flow particles move with local flow velocity between the two illuminations. The light scattered by the tracer particles is recorded on a single frame (Lavision camera with 1376×1024 pixels). The local displacement vector is determined for each interrogation area by means of statistical methods relating on correlation analysis with commercial software (Lavision Davis 7). It is assumed that all particles within one interrogation area have moved homogeneously between the two illuminations. The projection of the vector of the local flow velocity into the plane of the light sheet resulting in the two-component velocity vector is calculated taking into account the time delay between the two illuminations and the magnification at imaging.

4 Results and discussion

4.1 1D anemometry of round free jet

An axisymmetrical free jet issuing from a uniform circular extension tube as depicted in Fig. 2 with diameter d=25mm and varying length L_t is considered where the subscript t denotes the tube length in cm. The time averaged spatial velocity development is scanned with 1D anemometry mounted on a positioning system as outlined in section 3.2. The assessed extension tube lengths yield 1, 3, 9, 18 and 50cm corresponding to $L_t/d \in \{0.4, 1.2, 3.6, 7.2, 20\}$. Longitudinal data along the x direction are gathered from the tube exit up to $20d$. Radial profiles along the y direction are assessed near the tube exit and at 1.6, 3.2, 4, 4.8, 6.4, 8, 12 and $16d$. Varying the tube length L_t is a simple way to assess the influence of initial conditions corresponding to aging or articulation on the self-similar spatial jet development for a fixed volume flow rate of 130l/min or U_b=4.4m/s corresponding to $Re \approx 7350$. Exemplar time averaged statistics derived from the measured instantaneous velocity data are presented in Fig. 3. The mean longitudinal velocity profiles and exemplary mean radial velocity profile at x=3.2d are illustrated in Fig. 3(a) and 3(d). Both mean profiles prevail self-similarity as expressed in eq. 11 although the centerline decay constant K and model parameter α are seen to depend on L_t/d as shown in Fig. 4 for $K(L_t/d)$. The influence

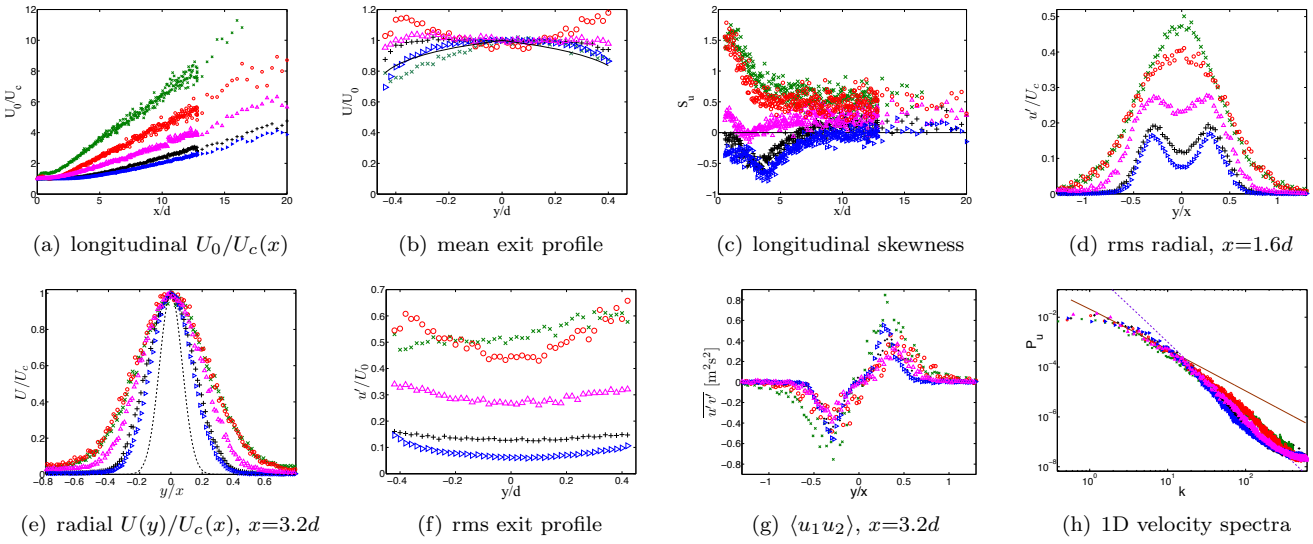

(a) longitudinal $U_0/U_c(x)$ (b) mean exit profile (c) longitudinal skewness (d) rms radial, x=1.6d

(e) radial $U(y)/U_c(x)$, x=3.2d (f) rms exit profile (g) $\langle u_1 u_2 \rangle$, x=3.2d (h) 1D velocity spectra

Figure 3: Exemplar velocity field characterisation for axisymmetric jet ($Re \approx 7350$) for L_t/d 0.4 ($\times$), 1.2 ($\circ$), 3.6 ($\triangle$), 7.2 ($+$) and 20 ($\triangleright$) cm. (b) full line: Blasius solution $U/U_c = (1-2y/d)^{1/7}$, (c) Gaussian distribution value (full) and (e) dotted line: Gaussian distribution of eq. 11 with α=94. (h) one dimensional velocity spectra at $x = 1.6d$ at maximum shear stress position $y/d \approx 0.7$. Kolgomorovs (full) and Kraichnans (dotted) law are modelled with eq. 15 with $n = 5/3$ and $n = 3$ respectively and dimensionless wavenumber $k = \omega d/U_c(x)$.

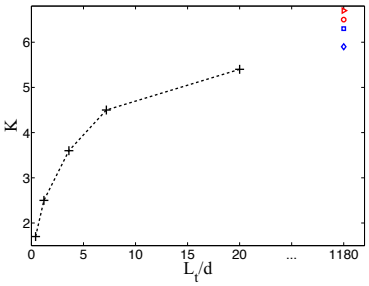

Figure 4: Decay rate $K(L_t/d)$ with long pipe values at $L/d = 1180$.

of L_t/d on initial conditions is illustrated in Fig. 3(b) for the mean and in 3(f) for the fluctuating part of the velocity. Except for L_t=1cm the initial mean velocity profile approaches Blasius solution $U/U_c = (1-2y/d)^{1/n}$ with $n = 7$ when L_t/d increases. The turbulence level at the exit increases from about 10 up to 60% of the centreline exit velocity when L_t/d is increased. The fluctuating centerline velocity can be characterised by its higher moments as illustrated for the centerline skewness in Fig. 3(c). The higher moments converge toward a constant value away from the exit for all assessed L_t/d. Moreover in the self-similar region this constant value approaches the value expected for a Gaussian distribution. The distance x/d needed to reach this constant value increases with L_t/d in consequence with the decreasing initial turbulence level. Moreover Gaussian values are seen to fit in particular for larger L_t/d. In accordance with the initial profiles the turbulence level decreases when L_t/d increases in the radial rms profiles as illustrated in Fig. 3(d). For the two smallest L_t/d the flow is turbulent from the exit, while for the larger L_t/d development of the shear layers is observed. The measured data are in agreement with the higher moments and mean centerline velocities indicating the absence of a potential cone for the smallest tube lengths L_t/d. A turbulent viscosity can be estimated for the flow following Eq. 12 from which the shear stress $\langle u_1 u_2 \rangle$ is derived as in eq. 13. From the exemplar shear stresses shown in Fig. 3(g) is seen that although the overall shape is the same, L_t/d and hence initial conditions influences the resulting shear stresses in several ways concerning the position, amplitude and width of the two peaks and as a consequence the slope between both peaks in accordance with the changes in $\nu_T(S)$ causing a stretching of the shear stresses. The one dimensional velocity spectra $P_u(k)$ at $x = 1.6d$ and maximum shear stress position $y/d \approx 0.7$ is illustrated in Fig. 3(h) for dimensionless wavenumber $k = \omega \cdot d/U_c(x)$. As for the shear stress the general shape is seen to be similar for all assessed L_t/d. The energy spectra are modelled following eq. 15 with $C_2 = 0.07$ for all spatial positions and all assessed L_t/d whereas C_1 varies with spatial position. Kolgomorovs power law $E(k) \sim k^{-5/3}$ describes well the inertial part of the spectrum while Kraichnans power law $E(k) \sim k^{-3}$ is seen to match the decay part. Hence the energy scales can be derived. Although in particular concerning the decay part a fine analysis reveals a faster decay for large L_t/d compared to small L_t/d and the same way the decay onset appears for slighty lower k-values for large L_t/d as for small L_t/d.

4.2 2D PIV

The characterisation presented in the previous section concerning a round free jet can be assessed in case 2D PIV data are considered. Resulting mean and rms are illustrated in Fig. 5 for a jet issuing from a circular tube with d=25mm as before, L_t/d=8.8 and $Re \approx 20000$. The flow through typical configurations of 'in-vitro' replicas depicted in Fig. 2 or 'in-vivo' articulator config-

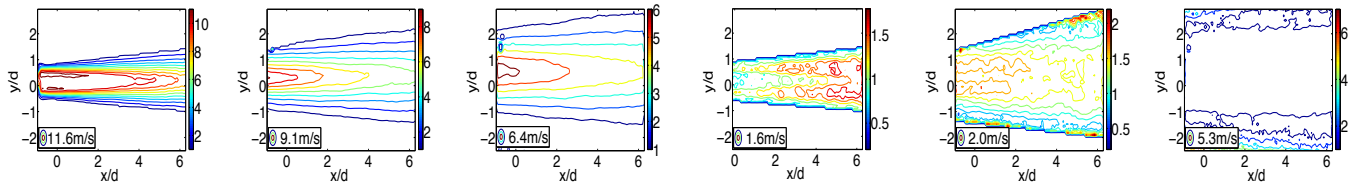

(a) mean (b) mean (c) mean (d) rms (e) rms (f) rms

Figure 5: Mean and rms 2D velocity distribution for round free jet ($Re \approx 20000$) for L_t/d=8.8: (a,d) exit up to x/d=6.8, (b,e) 6.8 up to x/d=13.6 and (c,f) 10.8 up to x/d=17.6.

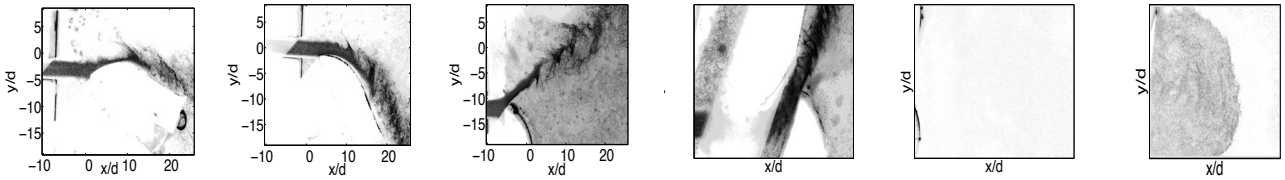

(a) 1 obstacle (b) 1 obstacle (c) 1 obstacle (d) 2 obstacles (e) closure (f) opening

Figure 6: (a,b,c,d) 2D PIV visualisation of jet interaction with downstream teeth shaped obstacles. (e,f) jet formation during auto-oscillation of deformable replica.

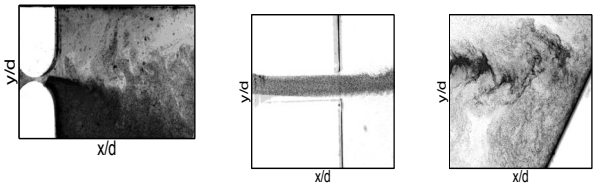

(a) round (b) uniform (c) impigement

Figure 7: 2D PIV visualisation of typical flow configurations: jet formation and surface impingement.

urations is qualitatively visualised in Fig. 7 for airflow through a round constriction, a uniform constriction and a jet impinging on a surface. Some more particular cases are illustrated in Fig. 6. In particular the interaction of the jet issuing from a uniform constriction with a downstream obstacle is illustrated. Different positions of the obstacle with respect to the jet as well as multiple obstacles are shown. Finally two images during a oscillatory cycle of the deformable replica taken at closure and opening are shown. Important issues such as flow separation and Coanda effect can be observed as well as the influence of the obstacle shape and placement.

5 Conclusion

Velocity field characterisation by means of 1D anemometry and 2D PIV is assessed quantitatively in case of a round free jet and qualitatively in case of constrictions and downstream obstacles likely to occur 'in-vivo'. The obtained visualisations indicate 2D PIV as an important tool to quantify flow-obstacle interactions relevant to typical vocal tract configurations.

Acknowledgments

The support of the French Rhône-Alpes Region (CIBLE 2006) and Agence National de la Recherche (ANR-07-JCJC-005) is gratefully acknowledged. Thanks for technical support at LEA: Laurent Philippon, Pascal Biais and Patrick Braud.

References

[1] H. Bruun. *Hot-wire anemometry.* Oxford Science Publications, New York, 1995.

[2] J. Cisonni, A. Van Hirtum, X. Pelorson, and J. Willems. Theoretical simulation and experimental validation of inverse quasi one-dimensional steady and unsteady glottal flow models. *J. Acoust. Soc. Am.*, Accepted, 2008.

[3] B. Erath and M. Plesniak. An investigation of bimodal jet trajectory in flow through scaled models of the human vocal tract. *Experiments in Fluids*, 40:683–696, 2006.

[4] S. Pope. *Turbulent flows.* Camebridge University Press, 2005.

[5] M. Raffel, C. Willert, S. Werely, and J. Kompenhans. *Particle Image Velocimetry.* Springer, New York, 2007.

[6] N. Ruty, X. Pelorson, A. Van Hirtum, I. Lopez, and A. Hirschberg. An in-vitro setup to test the relevance and the accuracy of low-order vocal folds models. *J. Acoust. Soc. Am.*, 121(1):479–490, 2007.

[7] H. Schlichting and K. Gersten. *Boundary layer theory.* Springer Verlag, Berlin, 2000.

[8] C. Shadle. *The acoustics of fricative consonants.* PhD thesis, 1985.

[9] K Stevens. *Acoustic Phonetics.* MIT Press, London, 1998.

[10] H. Vollmers. Detection of vortices and quantitative evaluation of their main parameters from experimental velocity data. *Meas. Sci. Technol.*, 12:1199–1207, 2001.